Surface characterization and microstructural evolution of railway rails in a medium-wide curve after preventive grinding

Schotsman, B.; Santofimia, M. J.; Petrov, R. H.; Sietsma, J.

DOI
10.1016/j.wear.2025.206237

Publication date
2025

Document Version
Final published version

Published in
Wear

Wear 580–581 (2025) 206237

Contents lists available at ScienceDirect

Wear

journal homepage: www.elsevier.com/locate/wear

Surface characterization and microstructural evolution of railway rails in a medium-wide curve after preventive grinding

B. Schotsman [a,b,*], M.J. Santofimia [a], R.H. Petrov [a,c], J. Sietsma [a]

[a] Delft University of Technology, Department Materials Science and Engineering, Mekelweg 2, 2628 CD Delft, The Netherlands
[b] ProRail, Moreelsepark 3, 3511 EP Utrecht, The Netherlands
[c] Ghent University, Department of Electrochemical, Systems and Metal Engineering, Technologiepark 46, Ghent, Belgium

ARTICLE INFO

Keywords:
Rail grinding
Preventive maintenance
Premium rail steel
Track test
Crack initiation

ABSTRACT

Preventive grinding of rails is a recurring maintenance routine to remove damage initiated in the wheel–rail contact. The grinding routine increases the service life of rails and reduces operational costs. Despite these benefits, grinding-related defects are observed. In this work a field test is performed to investigate the contact-surface formation and to better understand its durability. Surfaces after grinding are studied at different stages of the test to characterize wear mechanisms and deformation. The freshly ground surface exhibits a higher roughness and is composed of facets. It is determined that roughness asperities are extruded and fill grinding grooves in the process. High contact stresses at the facet transitions accelerate the extrusion of roughness asperities and the fast formation of the contact surface. The analysis further shows that deeper grinding grooves prevent homogeneous deformation. Strain concentrations arise due to the inhomogeneous deformation leading to damage initiation sites. These grooves are still present in the rail surface after the test. The evolution of the ground surface is captured in a schematic wear model.

1. Introduction

Traveling by train is safe and has low environmental impact, especially for high-speed long-distance travel. During the travel, the wheels of the train are carried and guided by steel rails which leads to wear and damage in the wheel-rail contact zone. In medium-wide curves, the formation of damages and the subsequent crack propagation in rails can be faster than the wear rate [1–3]. Therefore, the objective of preventive grinding is to remove these damage initiations and to restore the limited worn transverse rail head profile. Recurring grinding increases the rail service life and reduces operational costs [4–6].

Grinding of rails is typically a non-cooled process executed by systems equipped with multiple grinding motors that are placed vertically. The grinding wheels are shifted by grinding motor rotation to grind the entire rail head. Dedicated grinding patterns are developed for efficient performance [7–9]. When the grinding motor power is reduced in consecutive passes, surface quality and conformity with the target profile are further improved [9].

Despite the known benefits, the literature points to specific grinding-related surface features that may cause damage initiation after grinding [10–13]. Tribological and metallographic research on this topic is only available to a limited extent, although recent publications show a renewed interest [11,12,14,15].

The vertical placement of the grinding motors results in characteristic longitudinal strips on the rail head contour after grinding, which are called facets. Transition zones between the facets are associated with high contact stresses [8,14]. For instance, Fau et al. [13] observed flaking defects to arise from these zones.

During grinding, the material removal by cutting, ridge formation by plowing [16], the size distribution of the abrasive particles, and the orientation and protrusion height of these particles [17] cause a characteristic roughness profile. As a result, the first wheel contacts after grinding are on roughness asperities [18], causing material deformation, extrusion, and generally a high wear rate [19–21].

White etching layers (WEL) are formed after a temperature increase above A_{C3}, followed by rapid cooling [22]. Such high temperatures are achieved while grinding by the friction of the abrasive particles with most of the generated heat being transferred to the rail [23]. WEL are associated with various damage mechanisms. Rasmussen [12] observed that damage started at transverse, grinding-related, WEL stripes and Steenbergen [24] suggested that the damage initiates at WEL patches that are pressed into the microstructure. The grinding-related WEL

* Corresponding author at: Delft University of Technology, Department Materials Science and Engineering, Mekelweg 2, 2628 CD Delft, The Netherlands.
E-mail addresses: b.schotsman@tudelft.nl (B. Schotsman), m.j.santofimianavarro@tudelft.nl (M.J. Santofimia), roumen.petrov@ugent.be (R.H. Petrov), j.sietsma@tudelft.nl (J. Sietsma).

https://doi.org/10.1016/j.wear.2025.206237
Received 2 May 2025; Received in revised form 20 June 2025; Accepted 6 July 2025
Available online 21 July 2025

Fig. 1. The test site location. (a) Position in the south of The Netherlands. (b) At km 34.75 on the southbound track of the railway line Roermond-Sittard. (c) Site access from the level crossing *Roermondseweg*.

Table 1
Track lay-out and rail profile at the test site.

Rail profile	Curve radius	Cant	Cant deficiency
UIC54E5	1860 m	80 mm	25 mm

are typically thinner on high-strength rail steels compared to standard grade rail steels [25]. However, from high strength steels a smaller portion of the WEL breaks off compared to standard grades [15].

The objective of the present study is to better understand the relation between the ground rail surface characteristics, wear and deformation processes, and to evaluate the durability of the formed contact surface. For this purpose a field test was performed. A new rail was installed and subsequently in-situ ground to standard specifications for preventive rail grinding. For detailed studies of wear mechanisms and subsurface deformation, rail samples were extracted at different stages of contact-surface formation. The freshly ground rail surface was analyzed with special attention to transition zones, roughness, and WEL. The results of this field test provide new insights into wear mechanisms acting on the rail surface and the present study also identifies damage-promoting aspects of the ground surface condition.

2. Experimental details

2.1. Field test location and rail steel selection

Fig. 1 shows the location of the grinding field test. This location is selected because of its history of rail damage initiation, head checks and studs [26], accessibility for inspection, and moderate annual line load. The local train speed is 130 km h^{-1} and constant. Table 1 presents the relevant data of the track layout. The rail profile, curve radius, cant, which is the superelevation between the inner and outer rail, and the cant deficiency, provided the curve radius and train speed.

Table 2 shows the train traffic that passed the test site during the test. Trains were registered at the hot-bearing detector 5 km south of the test site. Axle load data from the closest weighing-in-motion measurement systems are coupled to these records. The table presents the cumulative and average axle loads, the latter accompanied by the standard deviation. Note that the typical local trains are short and equipped with 6 axles.

Table 3 shows the chemical composition and mechanical properties of the R370CrHT steel rail, subject of the current study. The R370CrHT is a fully pearlitic rail steel with chromium addition. The rail has a UIC54E5-stress relief profile [27], which is the common standard for curved track sections in the Dutch railway network. The pearlitic lamella thickness is 80 ± 3 nm [28].

The mechanical properties, determined in a monotonic tensile test as prescribed by the EN13674-1-standard [27], are shown in Table 3. The ultimate tensile strength, R_m, is defined as the engineering tensile strength. R_e is the 0.2%-offset yield strength. The plastic elongation at fracture, ϵ, is defined as the increase in length of the parallel section of the specimens. The relative area reduction, Z, is calculated from the measured diameter in the necked area. The hardness is determined at the centerline of the rail head after removing 0.5 mm from the surface.

2.2. Inspections and metallographic preparations

In the present experiment, the in-situ rail grinding was performed as part of the preventive grinding program before the monitoring started. A rail grinder, equipped with 64 grinding wheels for vertical-axis grinding, removed 0.2 mm of material in three passes at a grinding speed of 14 km h^{-1}, which is scheduled every 15 Mt. Before the experiment was completed, no further preventive grinding maintenance was carried out.

Locations for recurring inspections and measurements were marked and numbered. The inspection frequency and the extraction moments of the four rail samples were determined in a reference project. Inspections were carried out during the day, and measurements of surface roughness and hardness at night.

Table 4 presents the train load for the four rail samples, each with a length of 3 m. The coding of the samples consists of *rail sample (RS)* combined with the cumulative train load in Mt. A standard portable rail cutter with a 16 inch cutting blade was used to extract the samples. Manual grinding of the weld of the replacement rail was kept short and was marked to avoid mixing with the preventive grinding. The straightness of the running surface was measured to be within regulations, in order to minimize impact loading due to the additional welds in track. In addition, the sample locations were shifted against the direction of travel with increasing test duration, so that the rail surface to be studied is passed before the fresh weld.

Hardness measurements and surface roughness measurements on the rail surface were performed to quantify the progress of the contact surface formation. The surface roughness was determined in accordance with the EN-ISO4287 standard [29], using a Mitutoyo SJ210 surftester. The hardness was measured using a Equotip 3 Leeb rebound hardness tester, as described in the ASTM-A956 standard [30]. The resulting Leeb hardness was converted to Vickers hardness according to the ASTM-E140 standard [31]. Pictures of the contact surface were made with a 5 Mpx digital camera.

Table 2
Train traffic that passed the test site during the field test, from 29 March 2021 until 18 Dec 2021. The train traffic is divided into passenger trains, freight trains and other trains.

			Trains [#]	Axles [x10^3]	Cum. load [Mt]	Axle load [Tons]± σ
Measured trains	Passenger	Intercity	15 122	320	4.58	14.3 ± 1.4
		Local	9610	64.6	0.877	13.6 ± 1.9
	Freight		1519	124	1.75	14.2 ± 6.6
	Other		142	5.30	0.0608	11.5 ± 5.3
Total measured			26 393	515	7.27	14.2 ± 3.6

Table 3
Chemical composition (in wt%) and mechanical properties of R370CrHT rail steel as stated on the 3.1-certificate.

	C	Mn	Si	Cr	R_e (MPa)	R_m (MPa)	ϵ (%)	Z (%)	Hardness (HV)
R370CrHT	0.81	0.94	0.67	0.503	917	1319	12	42.1	426

Table 4
Rail samples (RS) extracted from the test site. The first row presents the rail sample codes, the second row the total load after grinding, and the third row the share of total load (%).

Rail sample	RS0	RS0.4	RS2.0	RS6.9
Total load [Mt]	0	0.43	2.04	6.92
Share of total load [%]	0	6.2	29.5	100

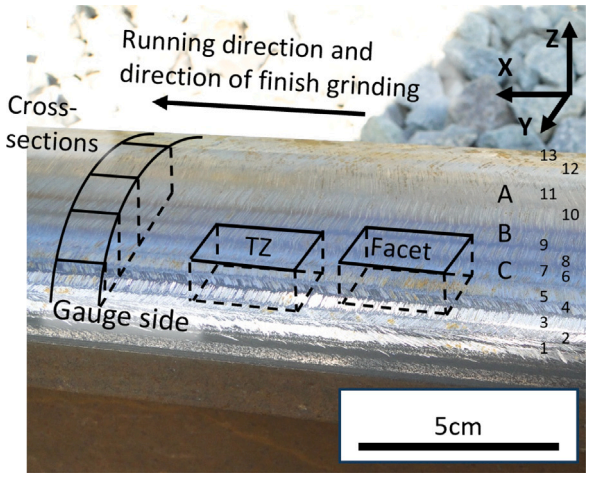

Fig. 2. Image of the ground in-service rail. At the rail surface are indicated: (1) Visually distinguishable ground facets (1–13). (2) Measurement positions for hardness and surface roughness measurements, A, B, and C. (3) The position of the metallographic sections: sections along the running direction at the facet and at the facet transition zone (TZ), and cross-sections.

Metallographic preparations started with a visual inspection of the sample surface. Pictures of the surface were made using the same 5 Mpx camera. Under lab conditions, the surface roughness and hardness were remeasured in agreement with the aforementioned standards at transverse positions A, B, and C, indicated in Fig. 2. Six connecting measurements were made, covering the characteristic length of the grinding process. Also six hardness measurements were performed, evenly distributed over the same sample length.

Fig. 2 shows the transverse and longitudinal micrograph positions for all four rail samples, which were cut after aligning the rail samples with respect to the ground facets and the characteristic length of the grinding pattern. Specimens were extracted from the middle of the facet and from the facet transition zone in the longitudinal direction. Cross-section specimens from the contact surface were cut into three parts to fit the 20 mm mold for specimen mounting.

The specimens were embedded in Struers ClaroCit Acrylic resin and prepared using a Struers MD-piano disc with 9 µm diamond polishing fluid, followed by polishing with 3 and 1 µm diamond polishing fluid. Specimens were etched with 2% Nital for 10 s. For optical microscopy a Keyence VHX5000 microscope was used. For detailed observations of the surface and the microstructure a JEOL IT100 Scanning Electron Microscope was used in secondary-electron detection mode with an acceleration voltage of 15 kV and 11 mm working distance.

3. Results

3.1. Characterization of the fresh ground surface

3.1.1. Surface analysis

Fig. 3a shows an optical micrograph of the rail surface of RS0 for detailed analysis. The grinding grooves are parallel and typical for vertical-axis grinding, formed transverse to the grinding direction. The average roughness is $R_a = 5.5 \pm 0.2$ µm. The pattern of repeated deeper grinding grooves evidences the characteristic length of the grinding process, which is ~67 mm.

Facets are smaller in the smaller-radius sections of the transverse rail head profile and wider in the larger-radius sections. The average width of the facets is 5±2 mm. Temper colors are an important quality indicator [32]. Blueing of individual grinding grooves is observed in facet 3, indicated with *i* in Fig. 3a, whereas in facet 12, see *ii*, groups of colored grooves are present. The purple to black surface oxidation in facet 7, see *iii*, is associated with temperatures above 735 °C, indicated as metallographic burn [33]. This burn is accompanied by WEL formation and these temperatures may even result in damage formation due to thermal stress [16,33,34].

Fig. 3b shows a SEM image of the blue-framed area in Fig. 3a, enclosing the facet transition zone. The width of the zone is ~800 µm and is defined by the variation in grinding groove lengths, as highlighted in the figure.

The deepest grinding grooves cross the transition zone and are often characterized by a different orientation. One such groove is indicated in Fig. 3c, which corresponds to the area enclosed by the red frame in Fig. 3a.

Fig. 3d presents the surface in the green-framed area of Fig. 3a and it encloses facet 7. Four characteristic features of the grinding grooves on facet 7 are:

- Cutting ridges are present at the bottom of the groove. In machining operations these ridges are associated with tool wear [16] and in grinding with the shape of the cutting face of the abrasive particles.
- Parallel grinding grooves, which display a mutual distance of ~80 µm caused by abrasive particles that simultaneously treated the surface.

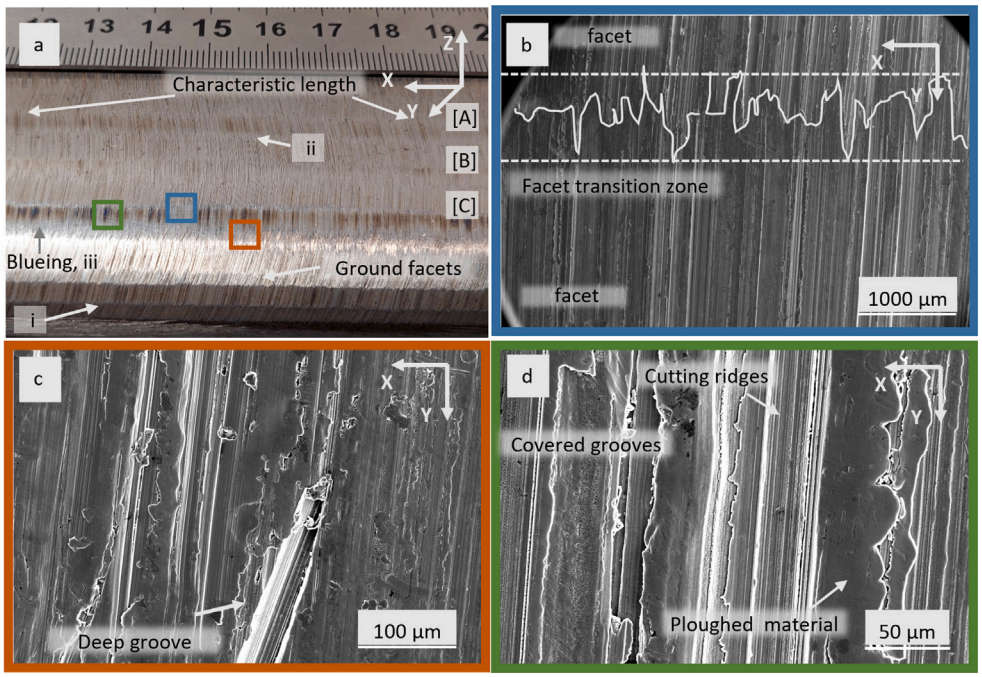

Fig. 3. Representative micrographs of the ground rail surface of sample RS0. (a) Optical micrograph of the ground surface. The measurement positions A–C, the characteristic length of the grinding process, and the various degrees of blueing, see *i-iii*, are indicated. (b) Facet transition zone. The extremities of the grinding grooves that define the transition zone are highlighted. (c) A grinding groove crossing the facet transition. (d) The characteristic grinding groove. Cutting ridges are present in the grinding grooves. At both sides of the groove plowed material is observed.

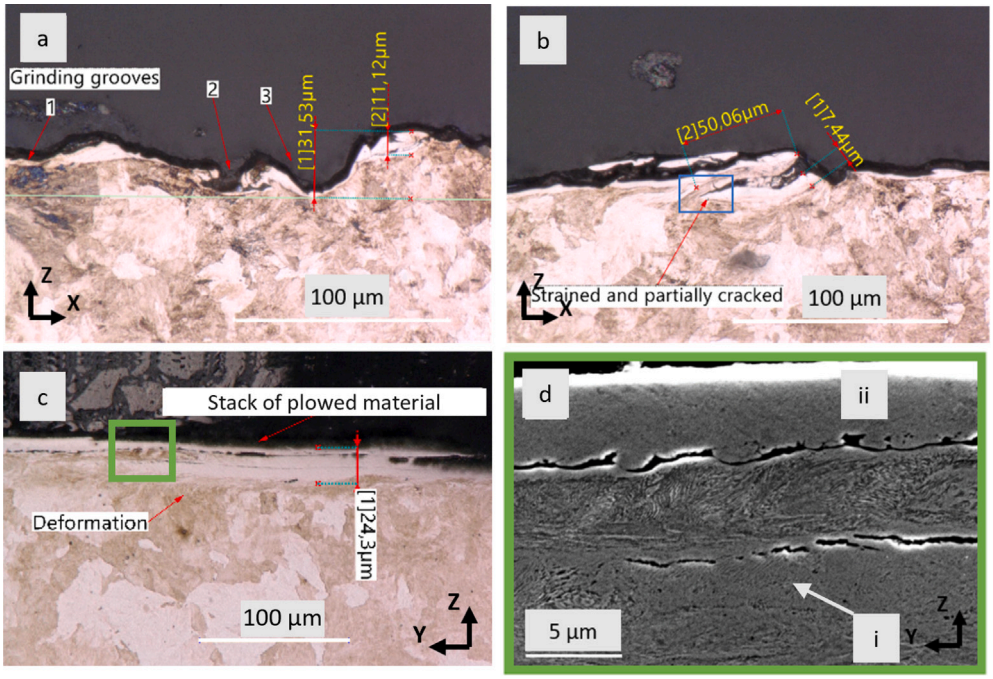

Fig. 4. The freshly ground rail surface observed in cross-section on metallographic specimens from rail sample RS0. (a) Grinding grooves with various widths and depths. Grinding groove 1 is shallow, grinding groove 2 is deeper and covered with extruded material, groove 3 is narrow and the distance to the ridge at the side is R_i ~31 µm. (b) Strained and partially cracked material that was not removed and covers the WEL-coated surface. (c) A stack of plowed material. The layers have a total thickness of ~24 µm. Below the layers, the deformation orientation is in the $-Y$-direction. (d) The SEM micrograph shows the green framed area in Fig. 4c in detail. The top layer is phase transformed, see *ii*. At the bottom, see *i*, a ~2 µm WEL is observed while the middle layer consists of strained pearlite with a small WEL at both sides.

- Plowing, which is characteristic for grinding [16] and causes material pile-ups or plowed ridges. At the $-X$-side, the material is plowed directly adjacent to the groove, whereas on the opposite side, several smaller frayed layers are present covering adjacent grinding grooves. The smooth surface texture of the plowed material is caused by the rubbing of the abrasive particle on the surface.

3.1.2. Cross-section analysis

Fig. 4 shows representative micrographs of RS0 to study the freshly ground surface. The micrograph in Fig. 4a is observed transverse to the running direction. It displays the variety of grinding groove profiles resulting from the abrasive particle size variation. The presence and orientation of extruded material in the parallel grinding grooves show

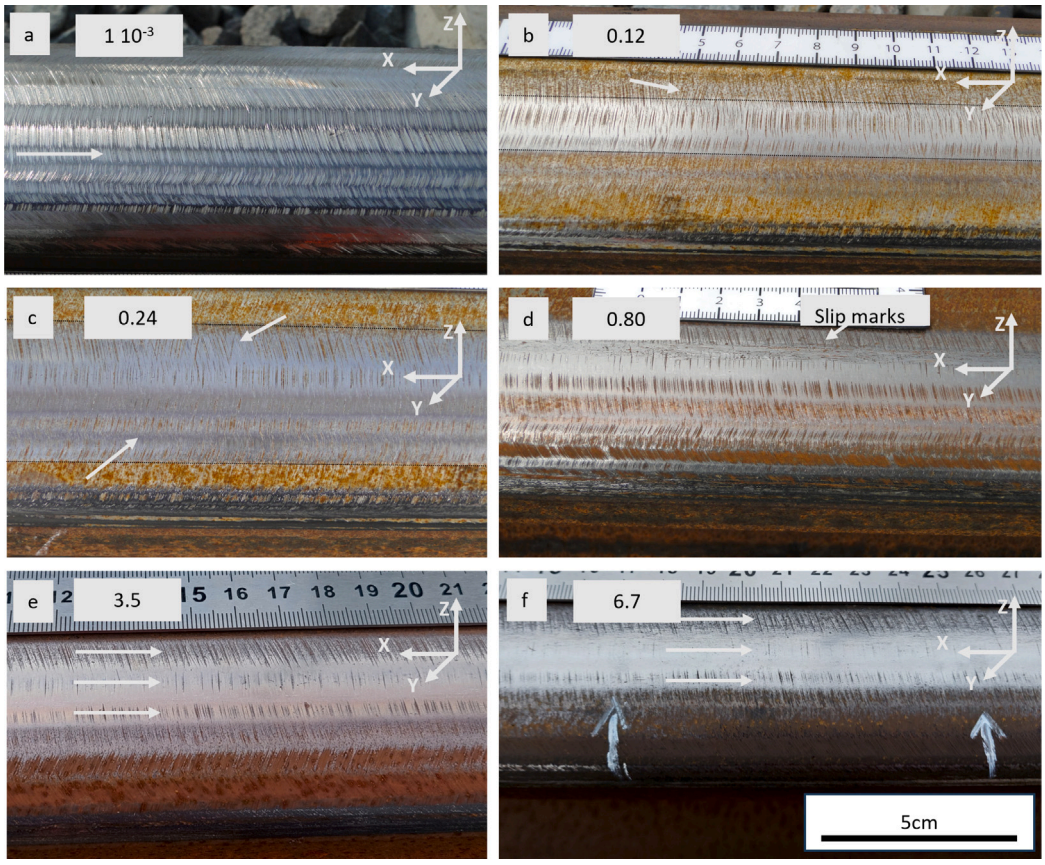

Fig. 5. The contact-surface formation as a function of the cumulative load, based on rail surface inspections in daylight. The cumulative load in Mt is presented in each micrograph. (a) 1×10^{-3} Mt. Contact-surface formation takes place at the facet transitions of facet 8, indicated by the arrow. Blueing from grinding is still present. (b) 0.12 Mt. Surface corrosion has taken place. The contact surface widens and load-carrying surfaces start to develop between the grinding grooves at the face surface. Grinding grooves with diverging orientations appear. (c) 0.24 Mt. The surface of the facet transitions is smooth on the gauge side of the contact zone. Surface corrosion is locally present at the facet surfaces and the grinding grooves with diverging orientation are still present. (d) 0.80 Mt. The contact surface width is reached and the corrosion layer has thickened. The length of grinding grooves shortens, but deeper grooves remain. Slip marks at the surface are caused by track maintenance and are not investigated. (e) 3.5 Mt. Three arrows are placed to observe the grinding groove lengths and the densities. (f) 6.7 Mt. The surface condition just before the field test is completed.

a cutting sequence, although the grooves were cut in the same grinding pass.

The same figure shows a detached WEL at the top of the ridges, possibly caused by frictional heat generated in the friction zone of the abrasive particle. Thin WEL is present at the bottom of the groove, resulting from frictional heating in the cutting zone. Fig. 4b shows another consequence of the cutting depth variation between abrasive particles. Material is strained instead of cut and removed, and is covering the freshly ground surface.

The observation direction in Figs. 4c and 4d is parallel to the running direction and perpendicular to the grinding grooves. Fig. 4c shows a material pile-up that results from subsequent passages of different abrasive particles plowing material to the side. The layers are shifted relative to each other due to different abrasive particle trajectories. The limited deformation below the pile-up, in the $-Y$-direction, evidences their direction of movement. In addition, some layers show evidence of WEL while other layers have remained pearlitic.

Fig. 4d presents a detailed SEM image taken within the green framed area of Fig. 4c. The strained pearlite of the middle layer has a ~1 μm thick WEL on both sides which is also present at the interface, see *i*. The surface layer, see *ii*, consists of WEL and the interface between the top layer and the pearlite middle layer is frayed. The protrusions seem to have deformed the pearlite microstructure.

3.2. Evolution of the ground rail surface during the field test

3.2.1. Surface evolution

Daylight inspections in track are performed at six stages of cumulative loading to evaluate the contact surface formation. Results of these inspections are presented in Fig. 5 for increasing cumulative loads. Wear patterns are interpreted as the qualitative indication for the wheel-contact locations.

Fig. 5a shows the rail surface after 1×10^{-3} Mt of load. The contact surface is narrow and facet transitions of facet 8, indicated by the arrow, are widening, evidencing localized contact.

In Fig. 5b the contact surface after 0.12 Mt is presented. The contact has widened and includes facet 9, which can be determined well by the surface corrosion that was worn away. In addition to the contact surfaces on the facet transitions, load-carrying surfaces develop on the facet surface, as evidenced by the surface widening between the brownish grinding grooves.

Fig. 5c shows that the contact width after 0.24 Mt of train load is wider than after 0.12 Mt. At the gauge side of the contact surface the wheel contact is concentrated at the facet transition zones, resulting in smooth and light gray surfaces.

The inspection results in Figs. 5d–f cover a longer period of time because the development of the contact surface, after the initial stage, occurs more gradually. The figures present the rail surface at 0.80 Mt, 3.5 Mt, and 6.7 Mt of train load, respectively. The contact surface width in Fig. 5d and in Fig. 5c is the same, from which it is deduced that the contact surface widening that took place during the initial stage of

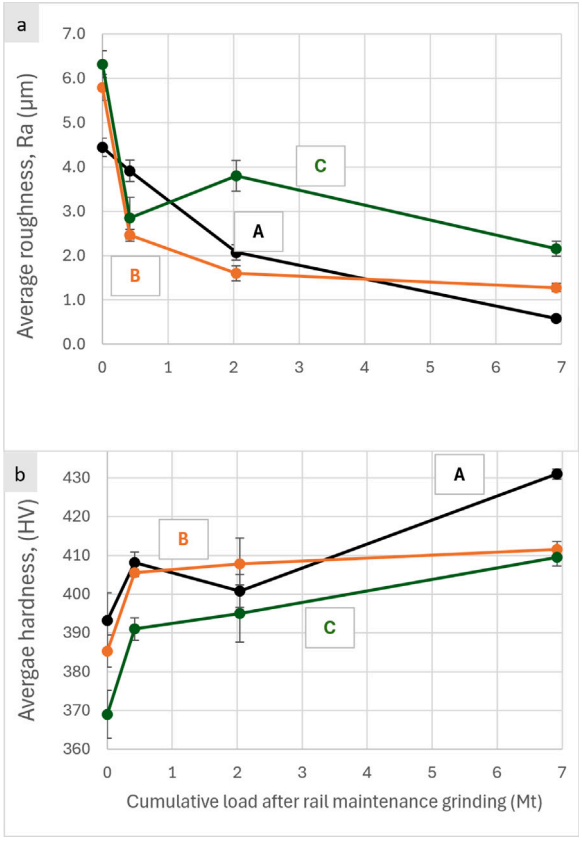

Fig. 6. The evolution of surface roughness (a) and hardness (b) in positions A, B and C, during the field test. The measurements were made on the surfaces of the extracted rail samples. See Fig. 2 for reference on the measurement positions.

the contact-surface formation stopped. The number of grinding grooves on the center of the contact surface decreases and the length shortens. Deep grooves are still present.

In order to compare the length and density of the remaining grinding grooves in Figs. 5e and 5f three arrows are placed at the same longitudinal and transverse positions relative to the characteristic grinding length and the facets. The comparison between both surface conditions shows for the middle arrow that the length and density of the remaining grinding grooves decrease and that some deeper grinding grooves remain. At the positions of both outer arrows, the length of the grinding grooves becomes only slightly shorter and the density remains almost the same.

3.2.2. Evolution of roughness, hardness and wear

The qualitative results of the track inspections are supported by measurements of surface roughness and hardness as shown in Fig. 6. Fig. 6a shows that the surface roughness initially reduces at a higher rate at measurement positions B and C. These positions are adjacent to facet 8, which is the facet that is the first to show facet-transition widening in Fig. 5a. At position A, at the center of the contact surface, the roughness initially decreases at a lower rate but eventually reaches the lowest surface roughness value.

The surface hardness is measured at the same positions A, B, and C to evaluate its development. The highest hardness is expected at positions experiencing the highest contact stresses. The results in Fig. 6b show that hardening proceeds initially fast at all measurement positions, but the highest hardness value of 431 ± 1 HV is reached, similar to the roughness, at position A.

Fig. 7 presents surface characteristics of wear mechanisms contributing to the contact-surface formation at the facet transition and at the facet. Fig. 7a shows the surface of RS0.4. At the facet, load-carrying surfaces were formed between the deeper grinding grooves, indicated with *i*, and at the facet transition zones virtually no grinding grooves are present, see *ii*. Fig. 7b shows the surface at *i* in detail. The surface is characterized by extruded slivers forming parallel lines. Deformation and sliver formation from roughness asperities is a known mechanism for surface roughness reduction [19,20]. In the process of sliver formation grinding grooves are covered and filled. The surface at *ii*, presented in Fig. 7c, is partially smooth and also similar parallel lines are present. The lines evidence a similar wear mechanism although the surface features may indicate a more advanced state of wear.

Fig. 7d shows the rail surface of RS6.9, after completion of the field test. A different form of wear has taken place at the surface in the orange-framed area. Wear slivers show serrated edges and have various orientations and lengths in Fig. 7e. These characteristics are associated with rolling contact fatigue damage initiation [1] rather than with wear tongue formation [35] or ratchetting-based wear [20].

3.2.3. Microstructure evolution

Until this point, the contact-surface formation on the ground rail surface has been analyzed using only surface observations. In Fig. 8 representative cross-section micrographs of the four rail samples RS0, RS0.4, RS2.0, and RS6.9 are presented in rows, including micrographs from the facet transitions and the facets in separate columns.

The freshly ground surface of RS0 shows, in the transition zone, a detached WEL patch on a relatively smooth surface with only one narrow grinding groove. The WEL shows no evidence of material removal, such as the presence of a groove, and is probably the result of rubbing by an abrasive particle on the surface. The facet surface seems to be formed by multiple abrasive particle contacts producing a roughness profile with various heights. This surface shows clear similarities with the surface presented in Fig. 4a, despite the different observation position.

Figs. 8c and 8d present the rail surfaces at RS0.4. In the transition zone, the mechanisms that contribute to the rapid formation of the contact surface are explained by three characteristic features. First, material extruded from the asperities covers grinding grooves, see *i*. Second, WEL formation takes place. The deformation and sharp transition between WEL and the pearlitic microstructure evidence the high temperatures that are reached during extrusion of asperities [36,37]. WEL is formed on both the extruded slivers and on adjacent areas, see *ii*. Third, subsurface deformation aligns with the direction of the traction, as highlighted by the dotted line. The deformation reaches a depth of ~60 µm and is only locally present, see *iii*. The facet surface is smooth and slightly wavy. At the facet no deformation or fresh WEL, associated with wheel load and slip, are observed.

Figs. 8e and 8f present the surfaces at sample RS2.0. At the facet-transition zone, the WEL thickness is smaller than that of RS0.4. The residual grinding groove in Fig. 8e, indicated with *i*, is partly covered with material from both sides. The second grinding groove, see *ii*, is filled with corroded material and damage initiates at the positive X-side. On the surface, next to the damage initiation, a fresh WEL has formed. The facet surface in Fig. 8f shows damage initiation at the extreme of the WEL, indicated with *i*, but the feature of interest is the large damage, see *ii*. A crack starts at the grinding groove bottom, bending downwards, and a parallel crack has initiated. Deformation, both at the surface and also below the surface, is concentrated at the positive X-side of the grinding groove.

Figs. 8g and 8h show the surface and deformation of rail sample RS6.9. The surface conditions at the facet and the transition zone are comparable and only the larger depth of deformation in the transition zone indicates a still slightly higher load.

In summary, the main observations on the formation of the contact surface are:

- Initially, the surface roughness at the transition zone exhibits a lower surface roughness than at the facet surface.

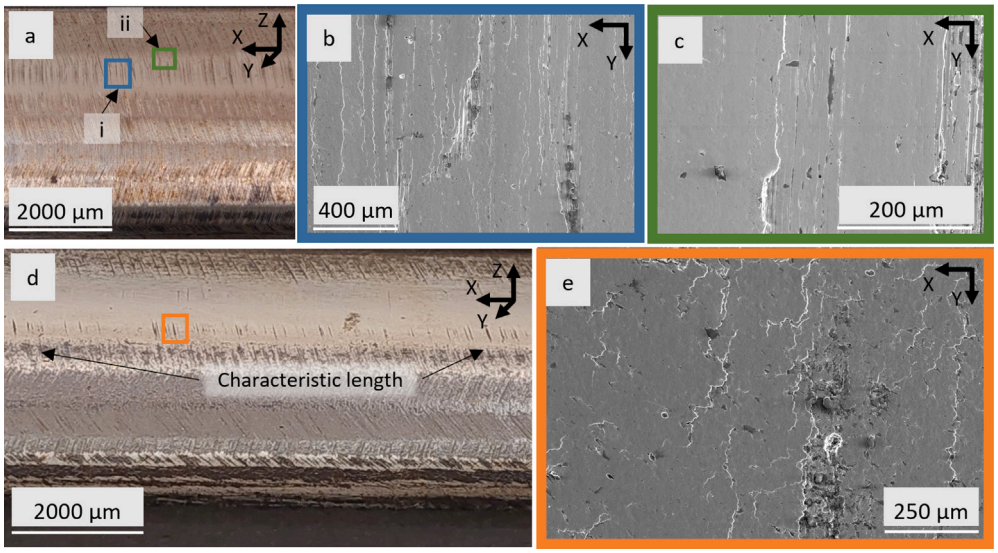

Fig. 7. The contact surface at rail sample RS0.4, a–c, and rail sample RS6.9, d–e. (a) Micrograph of the rail surface. Load-carrying surfaces develop between grinding grooves, see *i*, and the facet-transition zones are smooth, see *ii*. (b) On the facet surface in the blue frame, vertical lines and partly covered grinding grooves are present. Both are the result of extrusion of roughness asperities. (c) Extrusion lines on the surface in the facet-transition zone of the green-framed area. The parallel lines exhibit a lower density. (d) Micrograph of the rail surface. The middle of the contact surface is smooth but on both sides the deeper grooves remain. (e) The contact surface in the orange-framed area. The serrated edges of the lines on the surface exhibit various orientations and length. These are associated with rolling contact fatigue damage initiation.

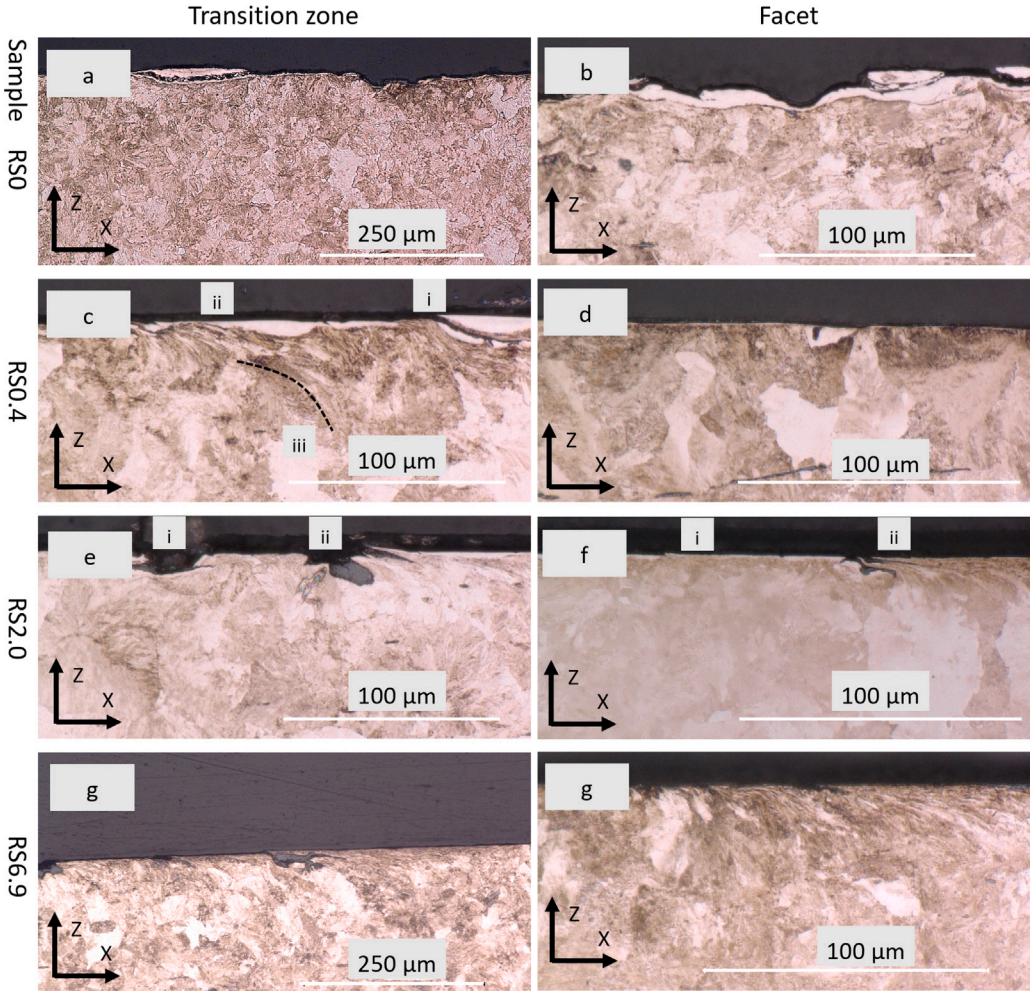

Fig. 8. The contact surface formation as observed on longitudinal sections. The rows of the array present the micrographs of sections from rail samples RS0 to RS6.9. The columns present the micrographs of sections from the transition zone position on the left and from the middle of the facet on the right. The microstructure details are described in the main text.

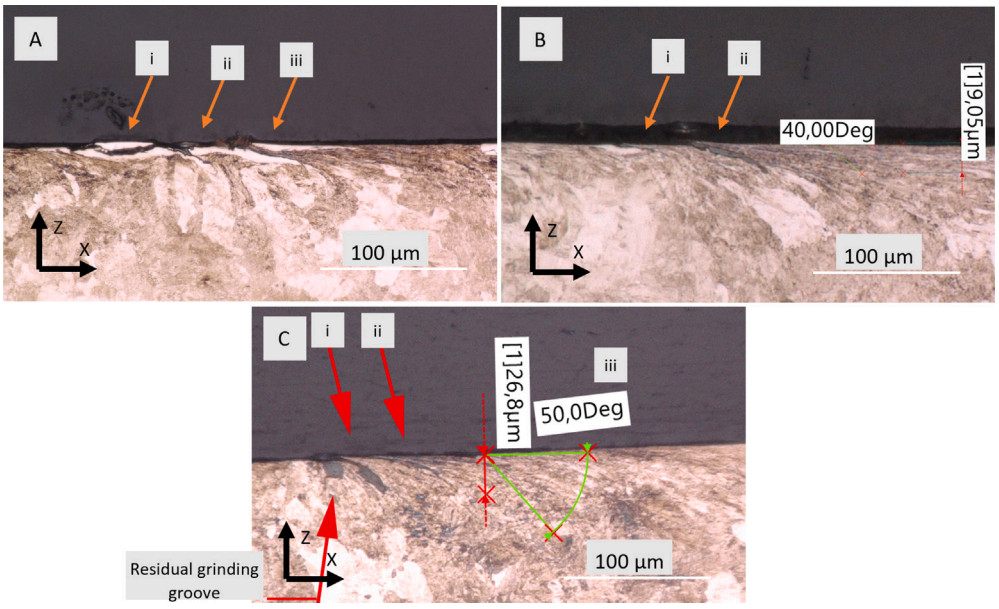

Fig. 9. Evolution of damage in the facet-transition zone of the rail surface. (a) RS0.4; the WEL in the grinding groove acts as a boundary for deformation and is submerged. The figure shows a detached WEL caused by grinding, see *i*. The freshly formed surface is partly embedded by material that has been extruded, see *ii*. A second extrusion is present which also traps the WEL at the surface. Here the deformation is more evident and a slip-related WEL has formed at the surface, see *iii*. (b) RS2.0; damage initiates at the surface. The WEL patch is pressed and embedded into the surface, see *i*. The crack that forms next to it reached a crack depth of 19 µm and the propagation orientation is 40° with respect to the surface, see *ii*. (c) RS6.9; at the surface two cracks are observed. One crack is present next to the residual grinding groove and is filled with corrosion products, see *i*. The second crack is closed and has a slightly shallower propagation orientation, see *ii*. The crack depth is ~27 µm and the propagation orientation is 50° with respect to the surface, see *iii*.

- The contact surface formation is assisted by asperity deformation covering grinding grooves. These observations confirm the occurrence of a ratchetting-based wear mechanism, as described by Akagaki and Kato [19] and Kapoor [20].
- Deformation and damage initiation occur mainly at one side of the grinding groove.
- The surface conditions of the facet transition and the facet after the grinding field test are the same.

3.3. Damage initiation

Previous sections showed that during contact-surface formation the presence of grinding grooves contributes to inhomogeneous deformation, extrusion of material and damage initiation. Fig. 9 highlights the evolution of the facet-transition zone surface under increasing cumulative load, evidencing damage initiation. Details of the microstructure, WEL and damage are described in the caption.

Fig. 9a presents the contact surface that was formed at the facet-transition zone of RS0.4. WEL patches are embedded and trapped in the surface, and deformation beneath the surface mainly takes place at the positive X-side of the grinding groove.

Fig. 9b presents the surface of RS2.0 to demonstrate the next stage of damage initiation. The surface crack, indicated with *ii*, is filled with corroded material and the crack faces are open. The crack propagates along the local deformation orientation and shows characteristics of both rolling contact fatigue and wear tongue formation.

Fig. 9c shows the surface of RS6.9 with two cracks, indicated with *i* and *ii*. Crack *i* is open and filled with corrosion products, which suggests that it initiated at a grinding groove. These grinding grooves form an obstacle for deformation, resulting in a locally deformed area. Crack *ii*, as a result, initiates in the zone of accumulated deformation.

4. Discussion

The formation of the contact surface formation on the freshly ground rail surface is studied under actual operating conditions. The inspections of the surface deliver valuable insights into the wear mechanisms and damage formation that take place.

4.1. The facet transition zones

Fig. 3a presents the freshly ground rail surface and Fig. 3b shows that the facets are connected by transition zones. During grinding with vertical-axis grinding systems, facets are formed on the rail surface that together approximate the contour of the rail head. The angle between the facets depends on the position on the head of the rail and is sharper at small radius sections and more obtuse at the top of the rail. This geometric deviation from the continuous rail contour causes contact stress concentrations at the transition zones which is, in the literature, indicated as a cause of damage initiation [13,15].

In this study it is observed that a contact surface is formed on the facet transition zones as soon as wheel–rail contact takes place, see Fig. 5a. As the contact surface widens and extends over multiple facets, the contact surface forms first at the transition zones of the facets added to the contact, see Fig. 5c. This contact surface-formation is faster at the transition zone compared to the facet itself because of the presence of locally high contact stresses and the local surface characteristics. These surface characteristics are determined by the grinding pattern whereby less material is removed in the transition zones than on the facet. Two aspects of rail grinding will be discussed briefly.

First, for all grinding process parameters being the same, a lower grinding depth results in a lower roughness height [16,38]. From analyses made by Kalpakjian, Schmid and Vijay Sekar [16] and Koshal [38] the following indicative relation between surface roughness, R_a, and grinding depth a_e was derived:

$$R_a \sim \frac{1}{4}\left(a_e\right)^{1/4}. \tag{1}$$

Second, the grinding pattern results in a lower metal removal at the facet transitions compared the facet itself. Kalousek et al. [8] presented a grinding pattern for efficient material removal using vertical axis grinding which are optimized using advanced simulation software [9]. The first grinding wheel forms a facet and each subsequent grinding wheel passage is then shifted and, as a consequence of limited angular shift, a part of the previously formed facet is removed. As a result,

the metal removal approaches zero at the side of the facet, forming the transition. By changing the inclination of the grinding motors, the differences in grinding depth between the facet and the facet transition are further increased, improving the grinding effectiveness and preventing the formation of circular grinding patterns on the rail surface.

The grinding pattern applied in the current study resulted in the presence of 13 observable facets on the final surface, as shown in Fig. 1, although in the grinding design even more facets are identified. The large number of facets requires a small grinding depth and results in even lower removal, and hence lower roughness, in the transition zones.

4.2. Wear transition

The observations of the contact surface in Figs. 7 and 8 show that the wear mechanism directly after grinding is ratchetting-based. Ratchetting is the repetitive loading of the material above the yield limit [20], eventually leading to failure.

Ratchetting-based wear models of rough surfaces successively describe asperity deformation, sliver formation, and sliver separation [20]. The practical applicability of these wear models can be tested experimentally by moving a hard slider over a softer surface, demonstrating the formation of parallel slivers from parallel asperities [19,39]. Akagaki and Kato [19] named this process of sliver formation 'flow wear'. The thin surface layers are progressively compressed and extruded, which is caused by contact stress concentration at the contact extremes [20].

Figs. 7b and c present the surface of RS0.4 evidencing the ratchetting-based wear. The parallel extruded slivers exhibit small mutual distances corresponding with the distances of the grinding grooves shown in Fig. 3d. Fig. 8c shows a micrograph of a facet transition of RS0.4. The slivers that are formed by extrusion cover and fill valleys in the ground surface, accelerating the reduction of the roughness. The direction of extrusion is determined by the tractive shear stresses that point in the $-X$-direction.

Fig. 7e shows the surface condition of RS6.9. The parallel slivers at the surface that were visible in RS0.4 are replaced by serrated lines and rolling contact fatigue (RCF) damage initiation has taken place.

When the contact surface is formed and the grinding roughness is removed, the wear rate becomes lower [40]. For a low wear mechanism like delamination wear to occur, platelets must be formed and removed from the rail surface. A process of void coalescence close to the surface has to take place, facilitating the detachment of the platelet [41]. For the formation of wear platelets a small crack propagation angle with respect to the surface is required, along with a tendency to develop upward branching cracks to cause detachment [1,42]. In contrast, RCF cracks tend to grow deep.

Wang et al. [1] performed two-disc experiments on eutectoid rail steel, applying a representative Hertz contact stress of 1161 MPa and slip ratios between 0.5% and 5% and found that crack growth exceeds the wear rate, independent of the slip ratio. They observed similar serrated lines at the surface which were ranked from 'coherent peeling' to 'tiny cracks' [1].

The expected wheel slip ratio at the railway steel in the test section is applied at the bottom of the slip range by Wang [1]. The surface condition as presented in Fig. 7e shows the best fit with the 1% slip ratio of the eutectoid rail steel surface.

4.3. WEL formation and deformation

In this work we propose a 5-stage wear model of the ground surface that captures the interactions between asperity deformation, WEL formation and the embedding of characteristic surface features, wear and damage initiation which is based on the observations in this experiment. Figs. 4a, 8c and 9 each show a portion of the overall development of the rail surface.

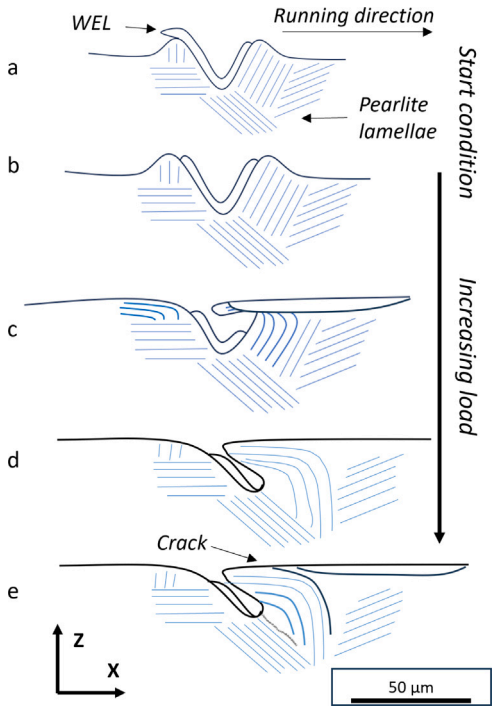

Fig. 10. Schematic model describing roughness reduction, and WEL removal, reappearance and submerging of the freshly ground surface.

Fig. 10 shows this schematic model for a simplified ground surface consisting of a representative single grinding groove and the adjacent surface. Fig. 10a presents the freshly ground surface. Material removal caused a groove with plowed ridges at both sides. The friction in the cutting zone caused heat generation resulting in a WEL at the bottom and at both sides, as well as the extrusion of material.

Fig. 10b represents the second stage. The majority of extruded slivers and semi-detached WEL patches are fractured and removed from the surface.

In Fig. 10c the load-carrying surface starts to form. Material is extruded, embedding ground surface features in the surface and the surface roughness is strongly reduced.

The material extrusion causes strain concentration at one side of the grinding groove. At the extruded material fresh WEL is formed. WEL, present at the surface of the grinding groove, spalls off from the deformed side but stays attached on the opposite side. During this stage the grinding groove starts to align with the deformation orientation.

Fig. 10d shows that, with the progress of the contact-surface formation, the reappeared WEL becomes thinner or is even worn off. The grinding groove, under ongoing deformation, is closed at this stage, resulting in flanks pressed together with the embedded WEL in between. Exposure to the elements causes the embedded WEL to corrode.

Fig. 10e shows the last wear stage. Wear processes at the surface have reduced the number of submerged grinding grooves, but the deepest grinding grooves still remain. Thin WEL reappears at the surface and damage initiates at the bottom of the deformed grinding groove and in the deformed material next to it.

The presented schematic model provides a comprehensive qualitative overview covering the characteristics of the freshly ground surface, the roughness reduction mechanisms and preferential damage initiation sites. Nevertheless, more research is needed to quantify the interrelation between the observed grinding groove characteristics and damage initiation.

5. Conclusions

A field test is performed to study the characteristics of the ground rail surface, wear and deformation processes, and to define critical aspects for the durability of the resulting contact surface. From the observations the following conclusions are drawn.

- The vertical-axis grinding forms facets at the rail profile. The width of the transition zones between facets is defined by the variation in grinding groove length. The contact stress at these facet transitions is initially high as a result of the rail head geometry. When the facet-transition zones are worn away, the surface and the subsurface deformation become similar for facets and facet transitions.
- A ratchetting-based wear mechanism contributes to the reduction of the surface roughness. Material from roughness asperities is extruded out of the contact, covers deeper grinding grooves and contributes to the fast formation of load-carrying surfaces. This wear mechanism is gradually replaced and crack initiation and propagation related to rolling contact fatigue starts to outgrow the wear.
- A schematic wear model is proposed to capture the observed interactions between deformation, white etching layers (WEL) formation and the embedding of ground surface features. After grinding WEL are present in the grinding grooves. First, spallation of extruded and phase-transformed material takes place. Subsequently crushing and submerging of grinding grooves occurs which is accompanied by the reappearance of WEL. Deeper grooves act as obstacles and prevent uniform deformation from occurring. Damage initiates adjacent to these grinding grooves in the zone with strain concentration.
- The study shows that deep grinding grooves introduce the risk of damage initiation from the ground surface. Deep grinding grooves are associated with high grinding depth, deformation, and burn. Depth variation in the grinding grooves is an inevitable characteristic of rail grinding. Despite the characteristic variations, deep grinding grooves should be avoided or fully removed by finishing passes. An acceptable depth seems to be defined by the material removal by wear during the formation of the contact surface.

CRediT authorship contribution statement

B. Schotsman: Writing – original draft, Visualization, Project administration, Investigation, Conceptualization. **M.J. Santofimia:** Writing – review & editing, Conceptualization. **R.H. Petrov:** Writing – review & editing. **J. Sietsma:** Writing – review & editing, Methodology.

Declaration of competing interest

The authors declare the following financial interests/personal relationships which may be considered as potential competing interests: Bart schotsman reports financial support was provided by M2i Materials Innovation Institute. If there are other authors, they declare that they have no known competing financial interests or personal relationships that could have appeared to influence the work reported in this paper.

Acknowledgments

This research was carried out under project number T18014 in the framework of the Partnership Program of the Materials innovation institute M2i (www.m2i.nl). We would like to thank ProRail, Netherlands for its financial support and Strukton Rail for the installation and replacement of the rails, and their support during inspections. The grinding work is executed by Speno International SA under the ProRail contract for preventive grinding.

Data availability

The raw/processed data and observations required to reproduce these findings are available on request.

References

[1] H.H. Wang, W.J. Wang, Z.Y. Han, Y. Wang, H.H. Ding, R. Lewis, Q. Lin, Q.Y. Liu, Z.R. Zhou, Wear and rolling contact fatigue competition mechanism of different types of rail steels under various slip ratios, Wear 522 (2023) http://dx.doi.org/10.1016/j.wear.2023.204721.
[2] J.E. Garnham, C.L. Davis, Very early stage rolling contact fatigue crack growth in pearlitic rail steels, Wear 271 (1–2) (2011) 100–112, http://dx.doi.org/10.1016/j.wear.2010.10.004.
[3] E. Magel, J. Kalousek, P. Sroba, Chasing the magic wear rate, in: Civil-Comp Proceedings, vol. 104, Civil-Comp Press, 2014, http://dx.doi.org/10.4203/ccp.104.116.
[4] E. Magel, M. Roney, J. Kalousek, P. Sroba, The blending of theory and practice in modern rail grinding, Fatigue Fract. Eng. Mater. Struct. 26 (10) (2003) 921–929, http://dx.doi.org/10.1046/j.1460-2695.2003.00669.x.
[5] R. de Vries, P. Sroba, E. Magel, Preventive grinding moves into the 21 st century on Canadian Pacific railway, in: Proceedings from the AREMA Annual Conference, Chicago, IL., 2001.
[6] P. Sroba, M. Roney, Rail Grinding Best Practices, Tech. rep., National research council of Canada, 2003.
[7] E.E. Magel, J. Kalousek, The application of contact mechanics to rail profile design and rail grinding, Wear 253 (2002) 308–316.
[8] J. Kalousek, P. Sroba, C. Hegelund, Analysis of rail grinding tests and implications for corrective and preventative grinding, in: Fourth International Heavy Haul Railway Conference 1989: Railways in Action, 1989, pp. 193–204.
[9] Q. Lin, J. Guo, H.Y. Wang, W.J. Wang, Q.Y. Liu, Optimal design of rail grinding patterns based on a rail grinding target profile, Proc. Inst. Mech. Eng. Part F: J. Rail Rapid Transit 232 (2) (2018) 560–571, http://dx.doi.org/10.1177/0954409716679447.
[10] S.L. Grassie, D.I. Fletcher, E.A. Gallardo Hernandez, P. Summers, Studs: a squat-type defect in rails, Proc. Inst. Mech. Eng. Part F: J. Rail Rapid Transit 226 (3) (2011) 243–256, http://dx.doi.org/10.1177/0954409711421462.
[11] M. Steenbergen, Rolling contact fatigue in relation to rail grinding, Wear 356–357 (2016) 110–121, http://dx.doi.org/10.1016/j.wear.2016.03.015.
[12] C.J. Rasmussen, S. Fæster, S. Dhar, J.V. Quaade, M. Bini, H.K. Danielsen, Surface crack formation on rails at grinding induced martensite white etching layers, Wear 384–385 (2017) 8–14, http://dx.doi.org/10.1016/j.wear.2017.04.014.
[13] F. Fau, H. Smith, S. Fretwell-Smith, L. Deng, Effect of grinding quality, lubrication quality and rail hardness on flaking defect initiation on high rails, in: Proceedings of the 10th International Conference on Contact Mechanics and Wear of Rail/Wheel Systems, CM2015, 2015.
[14] M. Mesaritis, M. Shamsa, P. Cuervo, J.F. Santa, A. Toro, M.B. Marshall, R. Lewis, A laboratory demonstration of rail grinding and analysis of running roughness and wear, Wear 456–457 (2020) http://dx.doi.org/10.1016/j.wear.2020.203379.
[15] M. Mesaritis, J.F. Santa, L.F. Molina, M. Palacio, A. Toro, R. Lewis, Post-field grinding evaluation of different rail grades in full-scale wheel/rail laboratory tests, Tribol. Int. 177 (2023) http://dx.doi.org/10.1016/j.triboint.2022.107980.
[16] S. Kalpakjian, S. Schmid, K. Vijay Sekar, Manufacturing engineering and technology, 7th SI edition, 2014.
[17] Z.B. Hou, R. Komanduri, On the mechanics of the grinding process - part I. Stochastic nature of the grinding process, Int. J. Mach. Tools Manuf. 43 (15) (2003) 1579–1593, http://dx.doi.org/10.1016/S0890-6955(03)00186-X.
[18] P.J. Blau, On the nature of running-in, Tribol. Int. 38 (11–12) (2005) 1007–1012, http://dx.doi.org/10.1016/j.triboint.2005.07.020.
[19] T. Akagaki, K. Kato, Plastic flow process of surface layers in flow wear under boundary lubricated conditions, Wear 117 (2) (1987) 179–196, http://dx.doi.org/10.1016/0043-1648(87)90254-7.
[20] A. Kapoor, Wear by plastic ratchetting, Wear 212 (1) (1997) 119–130, http://dx.doi.org/10.1016/S0043-1648(97)00083-5.
[21] A. Kapoor, F.J. Franklin, S.K. Wong, M. Ishida, Surface roughness and plastic flow in rail wheel contact, Wear 253 (2002) 257–264.
[22] V. Mattos Ferreira, M.G. Mecozzi, R.H. Petrov, J. Sietsma, Microstructure development of pearlitic railway steels subjected to fast heating, Mater. Des. 221 (2022) http://dx.doi.org/10.1016/j.matdes.2022.110989.
[23] S. Malkin, C. Guo, Thermal analysis of grinding, CIRP Ann 56 (2) (2007) 760–782, http://dx.doi.org/10.1016/j.cirp.2007.10.005.
[24] M. Steenbergen, Squat formation and rolling contact fatigue in curved rail track, Eng. Fract. Mech. 143 (2015) 80–96, http://dx.doi.org/10.1016/j.engfracmech.2015.05.060.
[25] A.D. Bedoya-Zapata, H. León-Henao, M. Mesaritis, L.F. Molina, M. Palacio, J.F. Santa, J.S. Rudas, A. Toro, R. Lewis, White etching layer (WEL) formation in different rail grades after grinding operations in the field, Wear 502–503 (2022) http://dx.doi.org/10.1016/j.wear.2022.204371.

[26] S.L. Grassie, Studs and squats: The evolving story, Wear 366–367 (2016) 194–199, http://dx.doi.org/10.1016/j.wear.2016.03.021.
[27] CEN, prEN13674-1 - Railway Applications - Rail - Part 1: Vignole Railway Rails 46 Kg/m and Above, European Committee for Standardization, 2023.
[28] S. Maya-Johnson, A.J. Ramirez, A. Toro, Fatigue crack growth rate of two pearlitic rail steels, Eng. Fract. Mech. 138 (2015) 63–72, http://dx.doi.org/10.1016/j.engfracmech.2015.03.023.
[29] CEN, ISO4287:1997 - geometrical product specification - surface texture: Profile method - terms, definitions and surface texture parameters, 1997.
[30] ASTM, A956 Standard Test Method for Leeb Hardness Testing of Steel Products, American Society of Testing Materials, 2022.
[31] ASTM, E140-12B Standard Hardness Conversion Tables for Metals Relationship Among Brinell Hardness, Vickers Hardness, Rockwell Hardness, Superficial Hardness, Knoop Hardness, Scleroscope Hardness, and Leeb Hardness, vol. 03.01, 2019.
[32] CEN, EN13231-3 - railway applications - track - acceptance of works - part 3: Acceptance of reprofiling rails in track, 2012.
[33] B. Lin, K. Zhou, J. Guo, Q. Liu, W. Wang, Influence of grinding parameters on surface temperature and burn behaviors of grinding rail, Tribol. Int. 122 (2018) 151–162, http://dx.doi.org/10.1016/j.triboint.2018.02.017.
[34] J. Wu, R.H. Petrov, S. Kölling, P. Koenraad, L. Malet, S. Godet, J. Sietsma, Micro and nanoscale characterization of complex multilayer-structured white etching layer in rails, Metals 8 (10) (2018) 749, http://dx.doi.org/10.3390/met8100749.
[35] G. Zhou, C. He, G. Wen, Q. Liu, Fatigue damage mechanism of railway wheels under lateral forces, Tribol. Int. 91 (2015) 160–169, http://dx.doi.org/10.1016/j.triboint.2015.07.008.
[36] R. Pan, Y. Chen, H. Lan, S. E, R. Ren, Investigation into the microstructure evolution and damage on rail at curved tracks, Wear 504–505 (2022) http://dx.doi.org/10.1016/j.wear.2022.204420.
[37] M. Steenbergen, R. Dollevoet, On the mechanism of squat formation on train rails - part I: Origination, Int. J. Fatigue 47 (2013) 361–372, http://dx.doi.org/10.1016/j.ijfatigue.2012.04.023.
[38] D. Koshal, Manufacturing Engineer's Reference Book, Elsevier, 2014.
[39] A.C.F. Cocks, A.R.S. Ponter, The plastic behaviour of components subjected to constant primary stresses and cyclic secondary strains, J. Strain Anal. Eng. Des. 20 (1) (1985) 7–14, http://dx.doi.org/10.1243/03093247V201007.
[40] P.J. Blau, Mechanisms for transitional friction and wear behavior of sliding metals, Wear 72 (1) (1981) 55–66, http://dx.doi.org/10.1016/0043-1648(81)90283-0, URL https://www.sciencedirect.com/science/article/pii/0043164881902830.
[41] N.P. Suh, The delamination theory of wear, Wear 25 (1973) 111–124, http://dx.doi.org/10.1016/0043-1648(73)90125-7.
[42] D. Zapata, J. Jaramillo, A. Toro, Rolling contact and adhesive wear of bainitic and pearlitic steels in low load regime, Wear 271 (1–2) (2011) 393–399, http://dx.doi.org/10.1016/j.wear.2010.10.009.